International Journal of Heat and Mass Transfer 53 (2010) 3585–3591

Contents lists available at ScienceDirect

International Journal of Heat and Mass Transfer

journal homepage: www.elsevier.com/locate/ijhmt

Numerical analysis and thermographic investigation of induction heating

Matej Kranjc, Anze Zupanic *, Damijan Miklavcic, Tomaz Jarm

University of Ljubljana, Faculty of Electrical Engineering, Trzaska 25, Ljubljana SI-1000, Slovenia

ARTICLE INFO

Article history:
Received 22 March 2010
Accepted 14 April 2010

Keywords:
Finite element method
Induction heating
Numerical analysis
Temperature measurement
Thermography

ABSTRACT

Induction heating process was investigated numerically and experimentally. Cylindrically shaped steel workpiece was heated with different heating protocols. Numerical model with coupled electromagnetic and thermal physical phenomena was solved using the finite element method. Temperature-dependent and temperature-independent steel material properties were considered and their impact on simulation results was evaluated. Simulation results were also compared with experimental measurements using an algorithm for processing thermographic images. Good agreement between them was obtained for workpieces without defects. With ability to observe temperature distributions and material defects, the thermographic camera demonstrated to be an effective non-contact measurement tool and suitable alternative to thermocouples.

1. Introduction

Induction heating is one of the most widely used methods for heat treatment of steel. It provides faster and more precise heating of local areas, consumes less energy and is considered environmentally friendlier than other methods. Other advantages also include lower labor cost for device operators, easy maintainability of the equipment, quality assurance, automation capability and high reliability [1].

Induction heating is a complex process including electromagnetic, thermal and metallurgic phenomena. In this process an alternating electric current induces electromagnetic field, which in turn induces eddy currents in the workpiece. The induced eddy currents release energy in the form of heat, which is then distributed throughout the workpiece. Preliminary numerical simulations of heat distribution are highly desirable in planning of induction heating systems, since choosing the right shape and position of the induction coil and adjusting the electric current properties to attain a desired temperature profile in the workpiece can be difficult. During the process of induction heating the temperature of the heated material changes on such a large scale that introduction of non-linear temperature-dependent material properties is necessary, especially when dealing with ferromagnetic materials [2]. Consequently, electromagnetic and temperature distributions are in most cases impossible to derive analytically, therefore numerical methods such as finite element method have been used extensively [3–5].

Experimental investigation of numerical models of induction heating is usually carried out by measuring the time course of temperature in the workpiece with thermocouples [6–8] or with thermographic cameras [9,10]. The main advantages of temperature measurement with thermocouples are: high precision of spot measurements, a possibility to measure internal temperature with sensors placed inside the workpiece and low cost. However, there are several difficulties associated with the use of thermocouples for measurement of temperature in large-volume workpieces. A large number of thermocouples placed inside the workpiece or on its surface can influence the process of induction heating. Furthermore, implementation of surface temperature measurements with thermocouples can be difficult to achieve on a production line. Another major constraint is the thermocouple's time response, since induction heating is a relatively fast process. To avoid these limitations, a non-contact measurement method based on thermography can be used. Thermography is a form of infrared (IR) measurement that provides a color-coded thermal profile of the target surface. Thermographic imaging devices, such as a thermographic camera, use focal plane arrays of sensors that respond to electromagnetic radiation in the IR range. Images or a video acquired by a thermographic camera can be stored for later studies or they can be processed in real-time. These data can also be used for detection of material defects in workpieces [11,12] or to observe temperature distributions and dynamic changes in the heating process, since modern thermographic cameras are able to track very rapid temperature variations in the microsecond domain.

In this paper induction heating of steel workpieces is described and investigated both numerically and experimentally. Initial comparison between temperature-dependent and independent steel material properties of the workpiece was made to determine the

---

* Corresponding author. Tel.: +386 14768347; fax: +386 14264658.
E-mail addresses: matej.kranjc@fe.uni-lj.si (M. Kranjc), anze.zupanic@fe.uni-lj.si (A. Zupanic), damijan.miklavcic@fe.uni-lj.si (D. Miklavcic), tomaz.jarm@fe.uni-lj.si (T. Jarm).

0017-9310/$ - see front matter © 2010 Elsevier Ltd. All rights reserved.
doi:10.1016/j.ijheatmasstransfer.2010.04.030

Nomenclature

A	magnetic potential vector
B	magnetic flux density vector
C	specific heat capacity
D	electric displacement field vector
E	electric field vector
H	magnetizing field vector
J	current density vector
Q	heat source
q_r	radiative heat flux
T	temperature
V	electric potential
v	velocity vector

Greek symbols

ε_0	dielectric permittivity of vacuum
ε_e	emissivity of the steel
λ	thermal conductivity
σ_s	Stefan–Boltzmann constant
ρ	material density
μ_0	magnetic permeability of vacuum

Subscripts

amb	ambient
dep	temperature dependent
indep	temperature independent

importance and relevance of temperature-dependent properties in the numerical model. An algorithm for processing thermographic data was developed and applied in the process of experimental investigation. Simulation and experimental results were evaluated and discussed.

2. Materials and methods

The workpiece used in our study was a non-ferromagnetic steel cylinder placed in the middle of a symmetric induction coil with four turns. Three identical cylindrically shaped workpieces measuring 250 mm in height and 50 mm in radius were used. As shown in Figs. 1 and 4 two ring-shaped and radially symmetric surface areas were chosen arbitrarily as the observation areas. The outer ring area extended between the radii of 20 and 23 mm, while the inner ring area extended between the radii of 13 and 18 mm from the central axis.

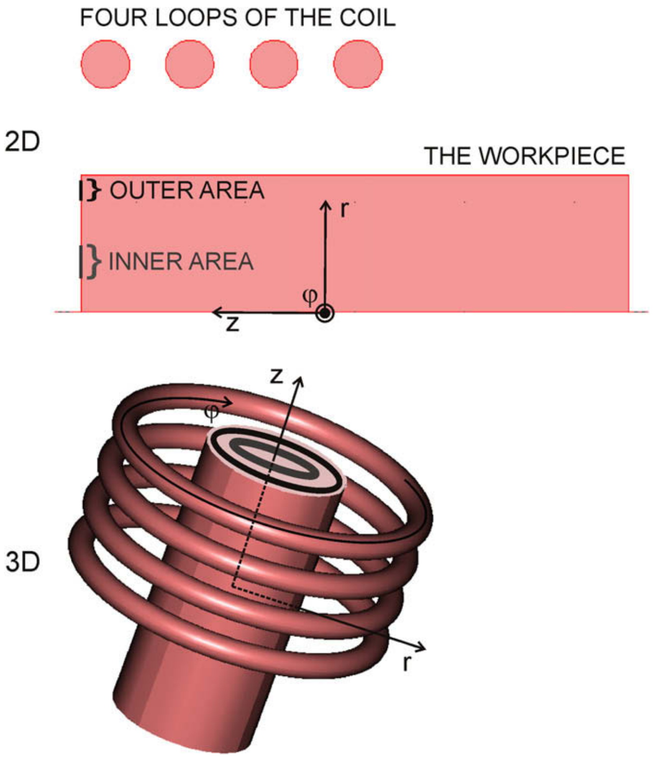

Fig. 1. Model geometry: cylindrically shaped steel workpiece surrounded by a coil of four loops placed in the cylindrical and in a three-dimensional coordinate system. The outer and inner evaluated areas are colored black and grey, respectively (see also Fig. 4). Due to symmetry only half of the workpiece is present in the cylindrical coordinate system.

Three different induction heating protocols marked 1, 2 and 3 (in the order of decreasing voltage) were used in our study. They differed only in the voltage used (higher voltage results in faster heating). The same frequency of 101 kHz was used with all protocols. Voltage values together with the resultant electric current amplitudes and frequency values are given in Table 1.

2.1. Properties of the steel workpieces

Uniform samples of a non-ferromagnetic steel X5CrNi189 (1.4301) were used as workpieces. This is one of the most widely used stainless steels with accurately determined physical properties. Three most important temperature-dependent material properties (the specific electric conductivity, the specific heat capacity and the thermal conductivity, respectively) of the steel were adapted from previous studies [13,14] and are presented in Fig. 2 and specified empirically in Eqs. (1)–(3).

$$\sigma(T) = 1/(4.9659 \times 10^{-7} + T \cdot 8.4121 \times 10^{-10} - T^2 \cdot 3.7246 \times 10^{-13} + T^4 \cdot 6.1960 \times 10^{-17}), \tag{1}$$

$$C(T) = 351.93 + T \cdot 976 \times 10^{-4}, \tag{2}$$

$$\lambda(T) = 11.215 + T \cdot 1.4087 \times 10^{-2}. \tag{3}$$

Simulations were performed for both the temperature-dependent and for the temperature-independent material properties. For temperature-independent properties the following constant values (measured at 25 °C) were used: $\sigma = 1.39$ (M S)/m, $C = 500$ J/(kg K), $\lambda = 16$ W/(K m). These values are presented in Fig. 2 and were obtained from the producer of steel samples used in our study (Metal Ravne, Ravne na Koroskem, Slovenia).

A constant value of 7900 kg/m^3 was used as mass density of the steel (ρ) in all simulations. The impact of these properties on the model was evaluated by examining the deviation D of results of the temperature-independent model from those of the temperature-dependent one in Eq. (4). This deviation was observed in the temperature range from 25 to 800 °C for the inner and the outer observation area of the workpiece.

$$D = \frac{T_{indep} - T_{dep}}{T_{dep}} \times 100\%. \tag{4}$$

2.2. Numerical model of induction heating

The problem was solved numerically in a cylindrical coordinate system due to axial symmetry of the geometry (see Fig. 1).

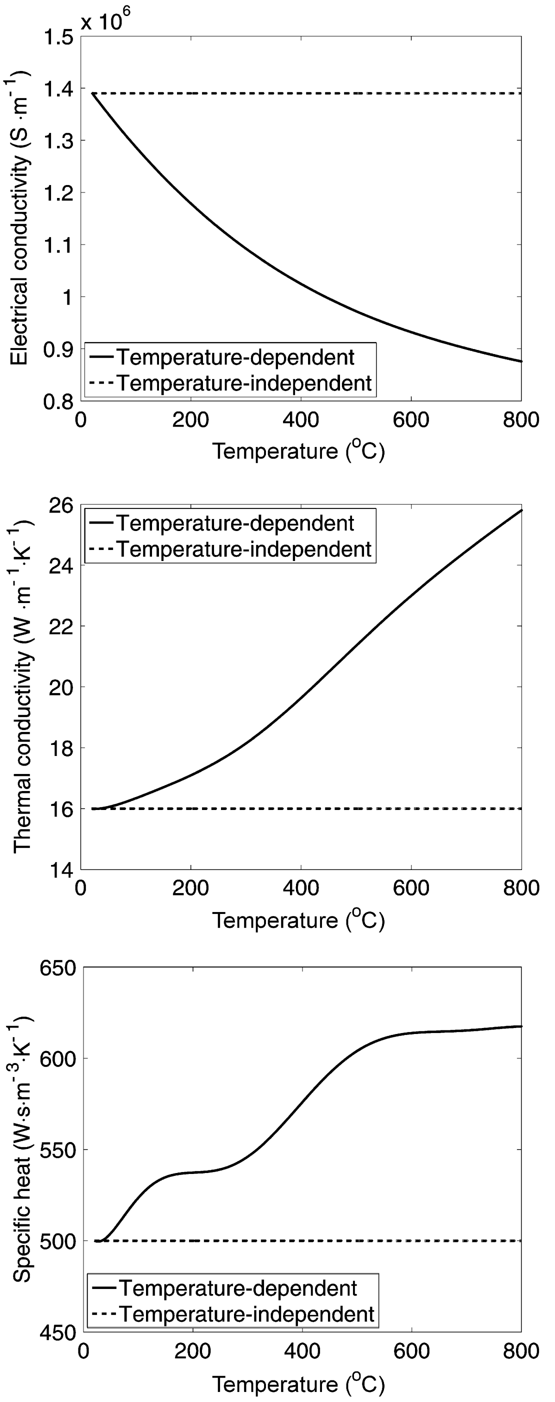

Fig. 2. Temperature-dependent and temperature-independent material properties of a non-ferromagnetic steel X5CrNi189. Values for the electrical conductivity, the specific heat and the thermal conductivity are shown.

Numerical calculations were performed with commercial finite element software package COMSOL Multiphysics 3.5a (COMSOL AB, Sweden) running on a desktop PC (Windows XP 64-bit, 3.2-GHz Intel Core i7 extreme, 12-GB RAM). The mesh of the numerical model consisted of 15,280 triangular elements and 61,435 degrees of freedom. The calculations took on average 10 min for the numerical model with temperature-dependent and 7 min for temperature-independent properties.

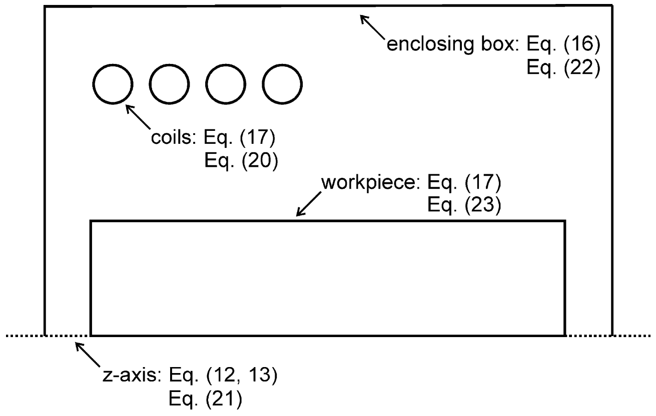

Fig. 3. Cylindrically-shaped workpiece surrounded by a coil placed in the cylindrical coordinate system with marked boundary conditions.

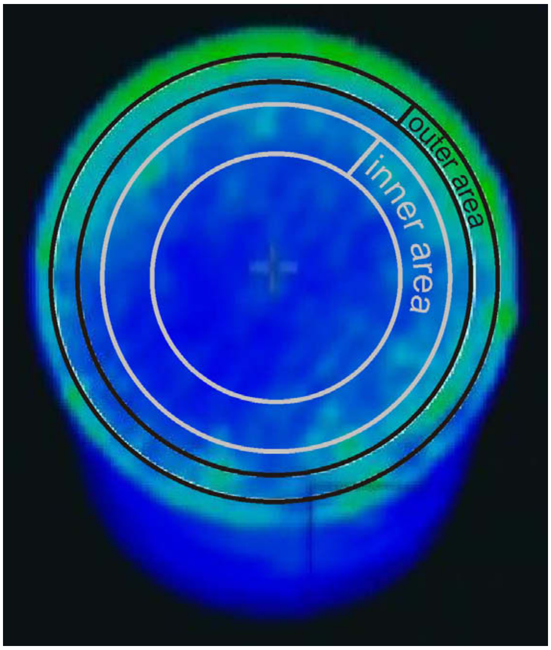

Fig. 4. Inner and outer radially symmetric ring-shaped surface areas, where the surface temperature was evaluated. The outer ring extended radially 20–23 mm (black) while the inner ring extended 13–18 mm (grey) from the central axis of the workpiece. The diameter of the steel workpiece was 50 mm.

Table 1
Parameters of the heating protocol in terms of the frequency of the applied voltage and the resultant electric current in the induction coil.

	Voltage amplitude (V)	Current amplitude (A)	Frequency (kHz)
Heating protocol 1	650	823	101
Heating protocol 2	450	608	101
Heating protocol 3	301	381	101

Mathematical equations describing the electromagnetic part are based on the Maxwell's equations. As the dimensions in the studied geometries are considerably smaller than the wavelength of the electromagnetic waves, a quasi-static approximation was used [15]. According to this approximation the Ampère's law can be written as

$$\nabla \times \mathbf{H} = \sigma(\mathbf{E} + \mathbf{v} \times \mathbf{B}). \tag{5}$$

Term $\mathbf{v} \times \mathbf{B}$ in Eq. (5) is assumed to be zero, considering the workpiece and the coil are both static. The relationship between magnetic and electric potential is introduced:

$$\mathbf{E} = -\nabla \mathbf{V} - \frac{\partial \mathbf{A}}{\partial t}. \tag{6}$$

The magnetic potential is a three-dimensional vector field, whose curl is equal to the magnetizing field, i.e.:

$$\mu \mathbf{H} = \nabla \times \mathbf{A}. \tag{7}$$

Substituting Eqs. (6) and (7) in Eq. (5) yields

$$\nabla \times \frac{1}{\mu}(\nabla \times \mathbf{A}) + \sigma\left(\nabla \mathbf{V} + \frac{\partial \mathbf{A}}{\partial t}\right) = 0. \tag{8}$$

After performing the double curl operation in the first term of Eq. (8) using the cylindrical coordinates defined by the set of unit vectors [$\mathbf{e_r}$, $\mathbf{e_\Phi}$,$\mathbf{e_z}$], the equation becomes a partial differential one. The magnetic potential is reduced to a single non-zero component $\mathbf{A} = A(r,z)\mathbf{e_\Phi}$ in the φ direction with the null divergence condition implicitly taken into account. Due to singularities of Eq. (8) along the symmetry axis where $r = 0$, an auxiliary variable u is introduced, defined for the non-zero component of magnetic field in the φ direction as

$$u = \frac{A_\varphi}{r}. \tag{9}$$

The term involving the gradient of electric potential can be written as

$$\nabla \mathbf{V} = \frac{V_{loop}}{2\pi r}, \tag{10}$$

where V_{loop} is the potential difference for one turn of the coil around the z-axis in the φ direction and therefore is present only in the region of the coil. Solving Eq. (8) in cylindrical coordinates and taking into account the considerations above, the problem is then to find u satisfying

$$\frac{r}{\mu}\frac{\partial^2 u}{\partial r^2} - 3\frac{1}{\mu}\frac{\partial u}{\partial r} - \frac{r}{\mu}\frac{\partial^2 u}{\partial z^2} + \sigma\left(\frac{V_{loop}}{2\pi r} + r\frac{\partial u}{\partial t}\right) = 0. \tag{11}$$

The boundary conditions for our model are presented in Fig. 3. For axial symmetry the following boundary condition along the z-axis must be used:

$$B_r = 0, \tag{12}$$

$$\frac{\partial B_z}{\partial r} = 0. \tag{13}$$

The first condition assures that the flow lines for the magnetic flux density begin at $r = 0$, while the second one prevents a discontinuity along the z-axis. Using the variable u, the boundary condition in Eq. (12) is fulfilled whenever r is zero:

$$B_r = -\frac{\partial A_\varphi}{\partial z} = -r\frac{\partial u}{\partial z}. \tag{14}$$

The second boundary condition Eq. (13) must be given explicitly. Using the variable u the following expression is obtained:

$$\frac{\partial B_z}{\partial r} = \frac{\partial}{\partial r}\left(\frac{1}{r}\frac{\partial}{\partial r}(rA_\varphi)\right) = r\frac{\partial^2 u}{\partial r^2} + 3\frac{\partial u}{\partial r}. \tag{15}$$

The expression is zero when r and the derivative of u with respect to r are both zero. The air surrounding the workpiece and the coil is enclosed in a box with magnetic insulation condition applied on its boundaries, which makes the normal component of the magnetic field zero:

$$A_\varphi = 0. \tag{16}$$

Boundary condition on the edges where the surfaces of the workpiece and coil meets the air is continuity:

$$\mathbf{n} \times \left(\mathbf{H}_{air} - \mathbf{H}_{coil/workpiece}\right) = 0. \tag{17}$$

Eddy currents derived from the electromagnetic model manifest themselves through heat production due to the Joule effect. The heat is then distributed throughout the workpiece. The process is described by a classical heat equation

$$\rho C\frac{\partial T}{\partial t} - \nabla(\lambda \nabla T) = Q. \tag{18}$$

The heat source Q is caused by the eddy currents:

$$Q = \frac{1}{2}\mathrm{Re}(\mathbf{J} \cdot \mathbf{E}^*). \tag{19}$$

As for the boundary conditions for the heat transfer model, continuity – Eq. (20) is imposed at the edges where the surface of the coil comes in contact with air. Thermal insulation – Eq. (21) is prescribed along the z-axis and specified temperature T_0 – Eq. (22) on the remaining edges of the box enclosing the whole numerical model. Also, surface-to-ambient radiation is imposed at the interface between the workpiece and air – Eq. (23) [16].

$$-\mathbf{n}_{air} \cdot (-\lambda_{air}\nabla T_{air}) - \mathbf{n}_{coil} \cdot (-\lambda_{coil}\nabla T_{coil}) = 0, \tag{20}$$

$$q = 0, \tag{21}$$

$$T = T_0, \tag{22}$$

$$q_r = \varepsilon_e \sigma_s (T_{amb}^4 - T^4). \tag{23}$$

2.3. Measurement setup

A thermographic camera was placed on a tripod above the vertically positioned steel workpiece to measure the temperature of its upper flat surface. The three different heating protocols were used (Table 1) and each workpiece was heated only once by one of the three heating protocols in order to avoid the influence of permanent changes in material properties caused by heating. The coil was driven by a high-power generator Ekoheat 45 (Ameritherm, Scottsville, USA). Surface temperature of the workpiece circular cross-section was measured with thermographic camera ThermoPro TP8 (AMETEK, Pennsylvania, USA) with the recording rate of 25 frames per second and the frame resolution of 576 × 720 dots. The camera was connected to a personal computer using Audio/Video device AverTV USB MCE (AverMedia, Taipei, Taiwan) via S-video connection cable. Emissivity of the steel workpiece was taken into account when calibrating the camera and was set to a constant value of 0.4 [17]. The accuracy of the thermographic camera was verified before the measurements by comparing the temperature values obtained with the camera and a thermocouple TM100 (Extech, Massachusetts, USA). Between several temperature ranges available on the camera the measurement range between 400 °C to 800 °C was chosen because temperatures below 400 °C are not interesting for heat treatment of steel. Due to the upper temperature measurement limit the process of induction heating was stopped when the maximum temperature in the workpiece reached 800 °C.

Video data were processed using Matlab R2009a Video and Image Processing blockset. As shown in Fig. 4 the video frames were masked with an appropriate template to isolate the ring-shaped inner and outer observation area of the upper flat surface of the steel bar, where the temperature was measured.

An algorithm from the Video and Image Processing blockset was used to compensate for the distortion of the workpiece surface area representation in the video (caused by the camera not being precisely aligned with the z-axis of workpiece) so that the correct circular shape was obtained. A moving average filter (length 15 frames) was used to smooth the video data by reducing the effect of electromagnetic interference present in the video recording. The data were further processed by an algorithm that compared the measured RGB values contained within the isolated ring areas with a generated full 24-bit RGB color scale based on the internal thermographic camera color scale. After temperature values of all pixels were obtained for all frames, the values were averaged in the inner and outer area for each single time frame to obtain a single temperature value later used in generating the time profile of heating.

3. Results

Temperature distribution in the workpiece calculated using the temperature-dependent properties is shown in Fig. 5 for heating protocol 1.

The difference between the simulation results using temperature-dependent and independent steel parameters are shown in Fig. 6 for three steel workpieces of equal dimensions heated using three different induction heating protocols (1, 2 and 3 – see Table 1).

In the outer observation area (the one closer to the surface of the workpiece) the deviation was very similar for all three heating protocols. The deviations were falling with the temperature approaching 230 °C. Above that value the deviations started to rise uniformly. However, in the inner observation area the deviations were remarkably more dependent on the heating protocol than in the outer observation area even though the general courses of deviation as a function of temperature were similar in both areas and for all three heating protocols. With the temperature approaching ~230 °C the deviations were larger in the inner compared to the outer observation area. Largest deviations were at 800 °C with the temperature difference of 14 °C and 23 °C in the inner and the outer area, respectively.

Fig. 7 shows a comparison of the results obtained by experimental measurement and numerical simulation using the temperature-dependent properties.

The temperature measurement range on the camera was set to 400–800 °C and therefore only this temperature range is shown. A good agreement between the results of numerical simulation and measurement are observed in workpieces for heating protocols 1 and 2 with the mean absolute difference of 3.2 °C and 9.7 °C in the outer area and 10.4 °C and 11.1 °C in the inner area, respectively. However, heating protocol 3 temperatures resulted considerably above those predicted by the model. The mean absolute difference of 31 °C and 37 °C for the outer and the inner ring respectively were found. An example of temperature distribution in the workpiece heated by protocol 3 is shown in Fig. 8.

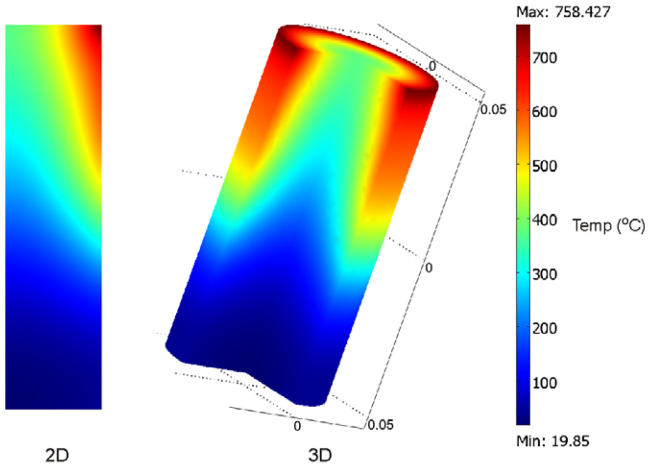

Fig. 5. Temperature distribution in the workpiece 55 s into heating by the heating protocol 1 presented as a 2D numerical model and the corresponding 3D model based on rotating the 2D model around the axis of symmetry by 270°. Due to high voltage frequency of 101 kHz temperatures near the thin layer under the surface reached higher values compared to those towards the center of the workpiece.

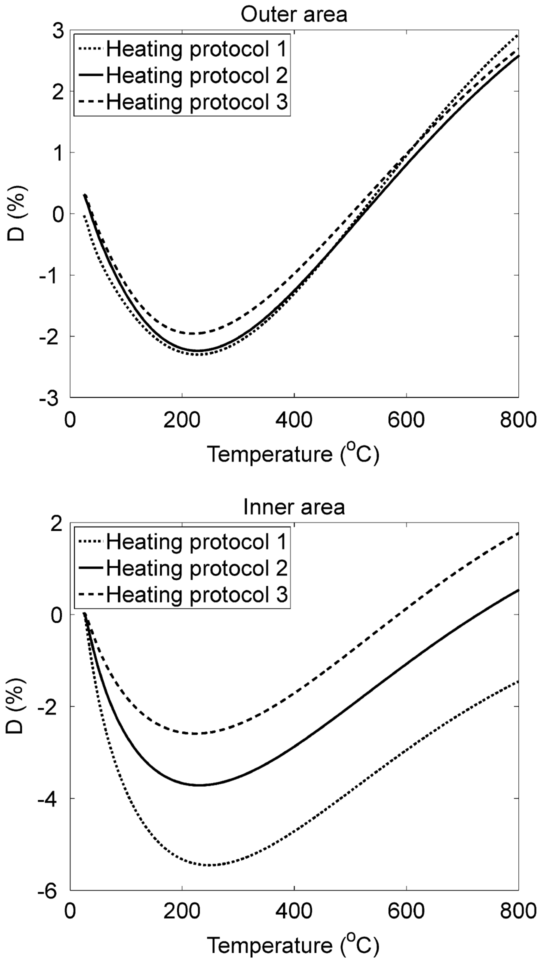

Fig. 6. Deviations between simulation results of numerical model with temperature-dependent and independent material properties of the workpiece. Temperature axis is based on temperature-dependent model. For easier comparison between temperatures in the inner and outer area simulations lasted until average temperature in the inner area reached 800 °C.

A lighter patch in the upper left corner indicates a material defect (inhomogeneity) in this workpiece and this is most likely the reason for relatively large difference in temperature between the measurement and simulation (note large temperature differences in the outlined regions belonging to two opposite sides of the workpiece).

4. Discussion

In our study of induction heating we compared the simulation results for temperature-dependent and temperature-independent material properties of a simple cylindrical-shaped stainless steel workpiece. Considerable differences between simulations were obtained and therefore temperature-dependent material properties are recommended to use when modeling induction heating. Numerical results were compared to measurements obtained by thermography, which proved to be an efficient and simple measurement method for relatively accurate assessment of temperature.

The comparison of simulations of induction heating using temperature-dependent and temperature-independent thermal conductivity, heat capacity and electrical conductivity showed considerable deviations. By increasing thermal conductivity (with

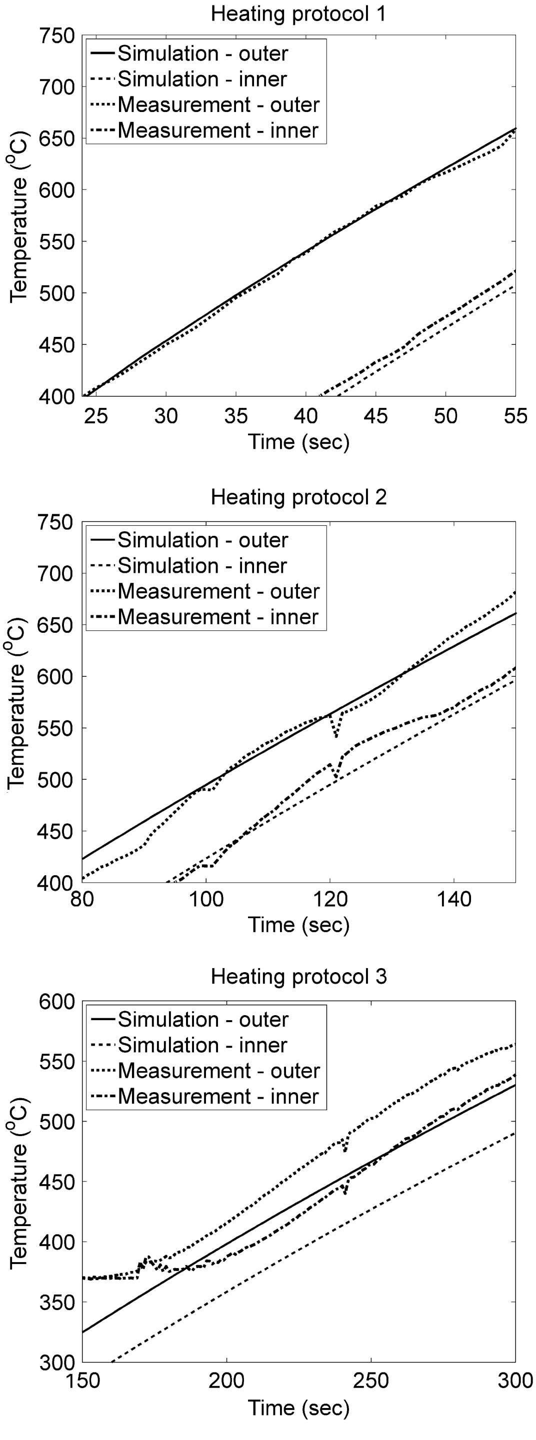

Fig. 7. Temperature in the inner and outer observation area as a function of heating time. The results of numerical simulation (using temperature-dependent parameters) are compared to those of experimental measurements using a thermographic camera for the three different heating protocols. The outer and inner surface area on the top of the steel cylinder consisted of concentric rings extending 20–23 mm and 13–18 mm from the central axis, respectively. Note that the data ranges (temperature and time) are different for the three heating protocols due to different speeds of heating.

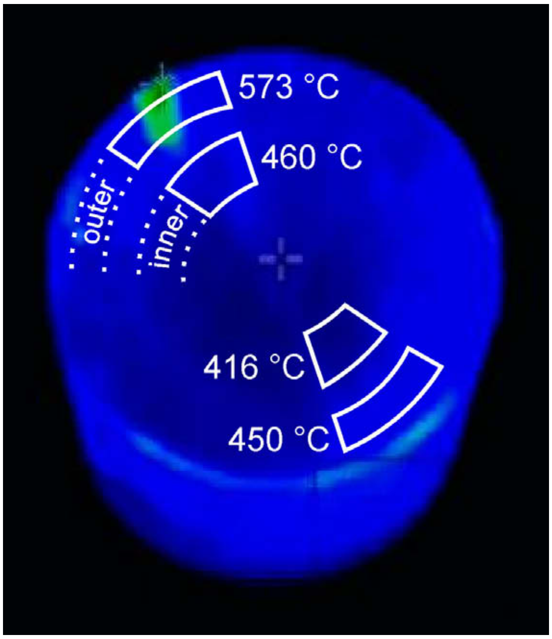

Fig. 8. A material defect or inhomogeneity (colored green) was observed with thermographic camera in the workpiece heated by protocol 3 (situation 240 s after the start of heating). Average temperatures in smaller portions of the outer and inner observation area are shown for comparison. (For interpretation of the references to colour in this figure legend, the reader is referred to the web version of this article.)

increasing temperature – Fig. 2) more heat can be dissipated from a thin layer under the surface of the workpiece, where it is generated, towards the center of the workpiece. Its influence is most clearly seen when temperatures approach 230 °C; the temperature-dependent model reaches higher temperatures compared to the temperature-independent model. Thermal dissipation is not as intense with heating protocol 3 as it is with protocol 1, which heats the workpiece the fastest. This can be observed in the inner area (Fig. 6) where the course of heating protocol 1 is farther above the course of protocol 3. Heat capacity also rises with temperature and therefore the temperature-dependent model predicts a larger amount of energy necessary to heat the steel compared to the independent model. The influence of heat capacity is observed in both areas (inner and outer), most notably when temperatures are above 230 °C as deviations between temperature-dependent and independent model start to decrease. Electrical conductivity decreases with temperature and therefore smaller currents are induced and less heat is generated in the temperature-dependent model. Its influence can be seen, mostly in heating of the outer area of the workpiece when temperatures are above 230 °C. As the electric current density decreases towards the center of the workpiece, influence of the electrical conductivity on heating of the inner area of the workpiece is negligible. To sum up, thermal conductivity influence is mostly seen when temperatures are approaching 230 °C and the temperature-dependent model reaches higher temperatures compared to the independent model. Above that temperature value temperature differences between dependent and independent model starts to decrease as heat capacity and electrical conductivity influences start to prevail over thermal conductivity. Use of the temperature-dependent material parameters also does not increase the computational time significantly in comparison to temperature-independent ones and therefore we conclude the temperature-dependent material properties should be used in the model whenever possible in order to increase the accuracy of the model.

A comparison between measurements and simulation of induction heating using temperature-dependent material properties was also made. A relatively good agreement between the two was seen for heating protocols 1 and 2, as can be observed in Fig. 7. There may have been minor measurement errors due to strong electromagnetic interferences caused by large electric currents in the induction coil which were present in individual video frames.

The impact of these interferences was reduced by averaging the consecutive video frames prior to video analysis. Further elimination of electromagnetic interferences could be attained with additional electromagnetic shielding of the equipment. The measurements could also be improved by using a thermographic camera with a larger temperature sensor to acquire more detailed thermographic images. Minor differences between numerical and experimental results can also be a result of inhomogeneities of the steel material and the dynamic emissivity value, which was not taken into account in measurements described in this paper. As emissivity of the material changes during heating due to surface deformation, a real-time measurement of emissivity value throughout the process of induction heating would be needed for more accurate results [18].

In the workpiece heated by heating protocol 3 a defect (large inhomogeneity) was observed with the thermographic camera as shown in Fig. 8. The defect has manifested itself in higher temperature values within its area in comparison to symmetrically located region on the opposite side of the workpiece. This material defect acted as an internal heat source and due to a long heating time of heating protocol 3 it affected the entire surface of the steel workpiece, including the inner and outer observation areas used for evaluation of heating profiles, by increasing the average temperature. Due to this material defect the difference between the results of the model and the measurements obtained for heating protocol 3 cannot be used for comparison with the model. On the other hand, the observed defect also demonstrated how useful the thermographic measurements can be for detection of material anomalies during heating [19].

Numerical models of induction heating can be used in numerous applications. One of the most prominent benefits of using a model is to reduce the time needed for design of new induction coils (inductors) for heating of asymmetric or otherwise geometrically complex workpieces or for achieving irregular heating patterns. Such an approach is particularly useful when specific requirements for different temperatures in different parts of the workpiece are required. Successful use of numerical models for such purposes, however, depends critically on their validation on experimentally measured temperature profiles. As use of thermocouples can sometimes be difficult, especially with complex geometries with limited availability of suitable areas for their placement, the non-contact approach using a thermographic camera can serve as a suitable alternative.

5. Conclusion

In this paper we report on investigation of induction heating of steel workpieces both numerically and experimentally. Initial comparison between numerical model with temperature-dependent and independent material properties showed important differences in the results and therefore temperature-dependent properties should be used whenever possible. The induction heating process was successfully investigated using a non-contact measurement method based on thermography. Thermographic measurements also demonstrated to be a useful tool for observing temperature distributions of workpieces during induction heating and for detection of material defects.

Acknowledgments

This work was in part financially supported by the Slovenian Research Agency (ARRS). Authors would also like to thank Mr. Branko Petric, B. S., the director and co-owner of Induktio d.o.o. (Ljubljana, Slovenia), a company that designs and manufactures induction heating devices, for making the experimental part of the study possible).

References

[1] V. Rudnev, D. Loveless, R. Cook, M. Black, Handbook of Induction Heating, Marcel Dekker, New York, 2003.
[2] B. Drobenko, O. Hachkevych, T. Kournyts'kyi, A mathematical simulation of high temperature induction heating of electroconductive solids, Int. J. Heat Mass Transfer 50 (2007) 616–624.
[3] F. Bay, V. Labbe, Y. Favennec, J.L. Chenot, A numerical model for induction heating processes coupling electromagnetism and thermomechanics, Int. J. Numer. Meth. Eng. 58 (2003) 839–867.
[4] O. Bodart, A.V. Boureau, R. Touzani, Numerical investigation of optimal control of induction heating processes, Appl. Math. Model. 25 (2001) 697–712.
[5] C. Marchand, A. Foggia, 2D finite-element program for magnetic induction-heating, IEEE Trans. Mag. 19 (1983) 2647–2649.
[6] J. Codrington, P. Nguyen, S.Y. Ho, A. Kotousov, Induction heating apparatus for high temperature testing of thermo-mechanical properties, Appl. Therm. Eng. 29 (2009) 2783–2789.
[7] H. Kurose, D. Miyagi, N. Takahashi, N. Uchida, K. Kawanaka, 3-D Eddy Current Analysis of Induction Heating Apparatus Considering Heat Emission, Heat Conduction, and Temperature Dependence of Magnetic Characteristics, IEEE-Inst Electrical Electronics Engineers Inc. (2009) 1847–1850.
[8] K. Sadeghipour, J.A. Dopkin, K. Li, A computer aided finite element experimental analysis of induction heating process of steel, Comput. Ind. 28 (1996) 195–205.
[9] M. Fabbri, M. Forzan, S. Lupi, A. Morandil, P.L. Ribani, Experimental and numerical analysis of DC induction heating of aluminum billets, IEEE Trans. Mag. 45 (2009) 192–200.
[10] M.-S. Huang, Y.-L. Huang, Effect of multi-layered induction coils on efficiency and uniformity of surface heating, Int. J. Heat Mass Transfer 53 (2010) 2414–2423.
[11] Y.S. Huang, J.W. Wu, Infrared Thermal Image Segmentations Employing the Multilayer Level Set Method for Non-destructive Evaluation of Layered Structures, Ndt&E International, vol. 43, 2010, pp. 34–44.
[12] M. Omar, M.I. Hassan, K. Saito, R. Alloo, IR self-referencing thermography for detection of in-depth defects, Infrared Phys. Technol. 46 (2005) 283–289.
[13] E.J. Davies, Conduction and Induction Heating, Peter Peregrinus, United Kingdom, London, 1990.
[14] C. Chaboudez, S. Clain, R. Glardon, D. Mari, J. Rappaz, M. Swierkosz, Numerical modeling in induction heating for axisymmetric geometries, IEEE Trans. Mag. 33 (1997) 739–745.
[15] J.A. Stratton, Electromagnetic Theory, Wiley–IEEE Press, New York, 2007.
[16] COMSOL, AC/DC module, User's guide, 2009.
[17] L. Gardner, K.T. Ng, Temperature development in structural stainless steel sections exposed to fire, Fire Safety J. 41 (2006) 185–203.
[18] V. Tank, H. Dietl, Multispectral infrared pyrometer for temperature-measurement with automatic correction of the influence of emissivity, Infrared Phys. 30 (1990) 331–342.
[19] M. Morbidini, P. Cawley, T. Barden, D. Almond, P. Duffour, Prediction of the thermosonic signal from fatigue cracks in metals using vibration damping measurements, J. Appl. Phys. 100 (2006).